Emadali, L., Motagh, M., Haghshenas Haghighi, M. (2017): Characterizing post-construction settlement of the Masjed-Soleyman embankment dam, Southwest Iran, using TerraSAR-X SpotLight radar imagery. - *Engineering Structures*, *143*, pp. 261—273.

DOI: http://doi.org/10.1016/j.engstruct.2017.04.009

Contents lists available at ScienceDirect

Engineering Structures

journal homepage: www.elsevier.com

Characterizing post-construction settlement of the Masjed-Soleyman embankment dam, Southwest Iran, using TerraSAR-X SpotLight radar imagery

Lotfollah Emadali[a], Mahdi Motagh[b, c, *], Mahmud Haghshenas Haghighi[b]

[a] School of Surveying and Geospatial Engineering, University of Tehran, Tehran, Iran
[b] GFZ German Research Center for Geosciences, Department of Geodesy, Section of Remote Sensing, 14473 Potsdam, Germany
[c] Institute for Photogrammetry and GeoInformation, Leibniz University Hannover, 30167 Hannover, Germany

ARTICLE INFO

Article history:
Received 23 July 2016
Received in revised form 29 March 2017
Accepted 5 April 2017
Available online xxx

Keywords:
Earthfill dam
Satellite radar
InSAR
TerraSAR-X
SpotLight

ABSTRACT

Geodetic monitoring of infrastructures is one of the key tasks in surveying and engineering geology. Systematic monitoring and assessment of the exterior deformation of embankment dams for safety analysis are often difficult when using classical surveying techniques due to time-consuming surveying procedures and high labour costs. Modern remote sensing techniques play an important role in efficiently assessing deformation: changes in the geometry, position and orientation of dams. In this study, we present the feasibility of effective post-construction deformation monitoring of the Masjed-Soleyman dam in Iran using high-resolution (~1 m) synthetic aperture radar (SAR) imagery in SpotLight (SL) mode from the X-band TerraSAR-X (TSX) satellite. This dam has been monitored over the last 15 years using classical surveying techniques, which provide horizontal and vertical deformation measurements of the structure. We show that high-resolution X-band SAR data provide a much more detailed identification of dam deformation in the crest and downstream that is not possible to infer from classical surveying techniques with few sparse geodetic monuments. High-resolution TSX data reveal that the dam is currently subject to two different deformation regimes: one is related to the crest and its adjacent area downstream, with a maximum rate of deformation of approximately 13 cm/yr in the radar line-of-sight (LOS). The other is related to the lower part of the downstream, with a maximum LOS velocity of 7 cm/yr. The effect of this centimetre displacement has been shown through several damage features on the dam body, including minor to large dislocation cracks on the crest and a significant deformation zone on the downstream slope.

1. Introduction

Embankment dams (earth and rockfill) are among the most important engineering structures built for the management of water resources in river basins for agriculture, flood control, and drinking water supply. They are subject to both internal and external loads that may induce deformation (displacement and strain) on the structure and its foundation. An embankment dam should be able to withstand static and dynamic loads imposed on it during its useable life. Generally, there are two types of deformation associated with embankment dams: the first is vertical subsidence caused by the weight of dam, and the second is horizontal deformation caused by the hydrostatic pressure of the reservoir, perpendicular to the main axis of the dam [1,2]. Deformation itself depends on various factors, including the water load of the reservoir, construction parameters (geometry, material, etc.), the water impoundment steps of the dam reservoir and the geological condition at the foundation of the dam [3,4].

Deformation monitoring at all stages of a dam's life is important for evaluating geometrical changes to the structure in space and time and deriving the relationship between causative factors and deformation [5]. Such an understanding is necessary for safety analysis, maintenance operation, and assessment of factors that could potentially deteriorate the dam, resulting in failure and a great risk for downriver areas [6–8]. Studies indicate that, on average, 10 significant dam failures occur globally every decade [9].

Periodic monitoring surveys with ground and satellite-based geodetic techniques are typically utilized to analyse the stability of dam structures [1,6,10]. Conventional surveying methods include a geodetic deformation network of a few reference points outside the dam body and a few object/deformation points on the body itself [7]. Object point position changes are then determined with respect to the reference points using various time periods of measurement. Despite the good precision, conventional surveying methods of deformation analysis are labour intensive and time-consuming when applied frequently over a large area for a long time period.

The rapid development of space technology over the last 20 years has allowed us to use the microwave remote sensing technique, Synthetic Aperture Radar Interferometry (InSAR), as an efficient and powerful geodetic method for analysing surface motion over thousands of kilometres associated with geophysical and anthropogenic processes [11–15]. However, the full potential of InSAR within the engineering community is still unrecognized. The importance of InSAR as a mature surveying technique in engineering geodesy and geology has further advanced in the last decade due to greater data

* Corresponding author at: GFZ German Research Center for Geosciences, Department of Geodesy, Section of Remote Sensing, 14473 Potsdam, Germany.
Email address: motagh@gfz-potsdam.de (M. Motagh)

http://dx.doi.org/10.1016/j.engstruct.2017.04.009
0141-0296/

availability from radar satellites and significant data processing improvements, allowing mm-accuracy monitoring of individual structures through multi-temporal analysis of radar images [16–19]. The development of high-resolution SAR imagery sensors aboard missions such as COSMO-SkyMed (CSK) and TerraSAR-X (TSX), together with a short revisit cycle (from 4 to 11 days), significantly improved our capabilities for infrastructure deformation analysis. High resolution SAR images can identify much higher density of point measurements in comparison to results from medium-resolution missions such as ERS and Envisat or ground-based surveying [20–25]. For example, Bovenga et al., 2012 [26] and Wasowski and Bovenga (2014) [27] documented an approximately 5 to 10 times higher density of measurements using CSK and TSX Stripmap data; the density of measurements often exceeded 1000 measurement points/km^2 in comparison with those obtained from medium resolution ERS and Envisat data. Even higher densities of measurements are obtained using SpotLight acquisitions [28,29]. For example, Bamler et al., 2009 [30], using SpotLight acquisitions, reported a density of more than 100,000 radar targets/km^2 for analysing ground deformations in urban areas.

This paper focuses on investigating the post-construction deformation of the Masjed-Soleyman dam in Iran using high-resolution X-band SAR data in SpotLight (SL) mode from the TerraSAR-X satellite. A 15-yr long surveying dataset is presented to show the long-term pattern of horizontal and vertical motion on the dam. Through interferometric observations from March 2014 to February 2015, we then quantify the recent magnitude and spatial pattern of dam deformation and compare the results with survey results for the same time period. The paper is organized as follows. In Section 2, we briefly explain the history of the Masjed-Soleyman dam. Section 3 describes the existing geodetic network and InSAR analysis used to assess deformation from X-band SAR data. The results of geodetic and InSAR surveys are presented in Section 4, followed by the Discussion and Conclusion in Sections 5 and 6, respectively.

2. The Masjed-Soleyman dam

The Masjed-Soleyman dam was constructed between 1995 and 2000 on the Karoun River, which is one of the largest and longest rivers in Iran (length ~ 950 km) and one of the most important surface water resources in the country. The watershed area is estimated to be approximately 60,000 km^2. The dam is located approximately 25 km northeast of Masjed-Soleyman City in the Khouzestan province of southwestern Iran (Fig. 1).

The Masjed-Soleyman dam is an embankment dam (rockfill) with a vertical central clay core. The height of crest above foundation is 177 m, with a crest length of 497 m and a crest width of 15 m. The width from heel to toe is 780 m, and the slope of embankment is 1 to 2 for upstream and 1 to 1.75 for downstream (Fig. 2). The embankment component aggregates, which vary in size from sand to gravel, consist primarily of sedimentary (limestone, sandstone and shale) rocks. The dam power station has the potential to produce 2000 MW from eight units, each with a 250 MW capacity. This dam has the largest spillway in Iran with a capacity of 21,700 m^3/s.

The first water impoundment of the reservoir was in December 2000 (one month after the construction completion) at a level of 254.8 m. In the following two years, the water level in the dam reservoir rose approximately 99 m, from 254.8 m in December 2000 to 306.5 m in December 2001 and to 353.7 m in December 2002. The water level was then further increased to 370 m in December 2003, with no significant subsequent change (Fig. 3).

Soon after the first impoundment of the dam, cross and longitudinal cracks started to develop in the dam crest, especially at the junction of concrete or steel elements to the rockfill dam shell. Because of these deformations, monitoring of Masjed-Soleyman dam became particularly important.

3. Geodetic data

3.1. Surveying network of the dam

As of 2000, a terrestrial surveying network was established on and around the dam, and so far, 15 consecutive measurements have been performed on this network. The main network on the dam (crest and downstream slope) includes 25 target points on the dam body. With high-precision total station theodolites horizontal distances, bearings and vertical angles were measured with respect to six off-dam pillars as fixed control points. The nominal angular precisions of 0.5″ and 1 mm + 1 ppm were set for measuring angles and distances, respectively. The height difference between the stations was measured using digital levels with a nominal precision of 0.3 mm/km.

The location of the geodetic points (on-dam network) is illustrated in Fig. 4. All measurements were adjusted using an over-constraint least-squares adjustment [31] to derive horizontal coordinates of the surveying points in each time period. Coordinate differences were then computed for every station to derive horizontal motion. The height-difference measurements were also adjusted using a least-squares technique to estimate the point heights with respect to the BM5 levelling benchmark as illustrated in Fig. 4.

For comparison with InSAR data (Section 3.2), we used only part of the results obtained from terrestrial surveying, the 2014–2015 time period, which corresponds with the InSAR data. The surveying cam-

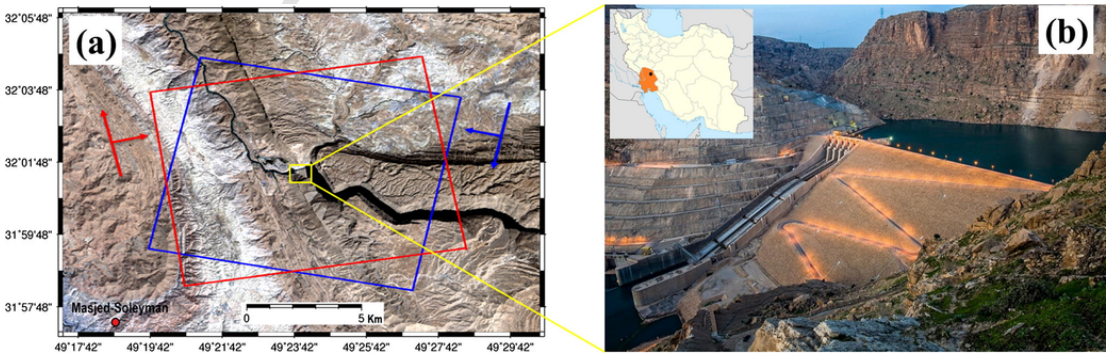

Fig. 1. (a) Google Earth™ image of the study area. Yellow rectangle delineates the location of the Masjed-Soleyman dam. Blue and red rectangles correspond to the frame covered by descending and ascending TerraSAR-X data. (b) View of the Masjed-Soleyman dam facing downstream. The inset shows the location of the dam in Iran. (For interpretation of the references to colour in this figure legend, the reader is referred to the web version of this article.)

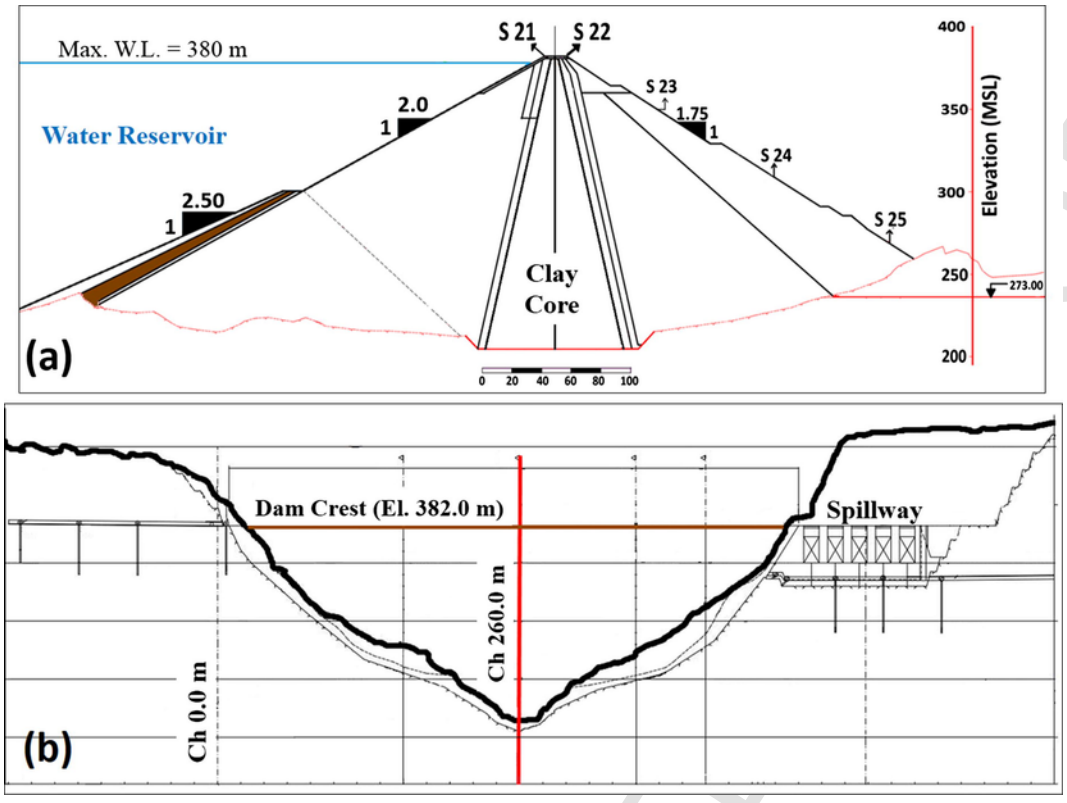

Fig. 2. (a) Cross-section of the dam. (b) Longitudinal section of the dam.

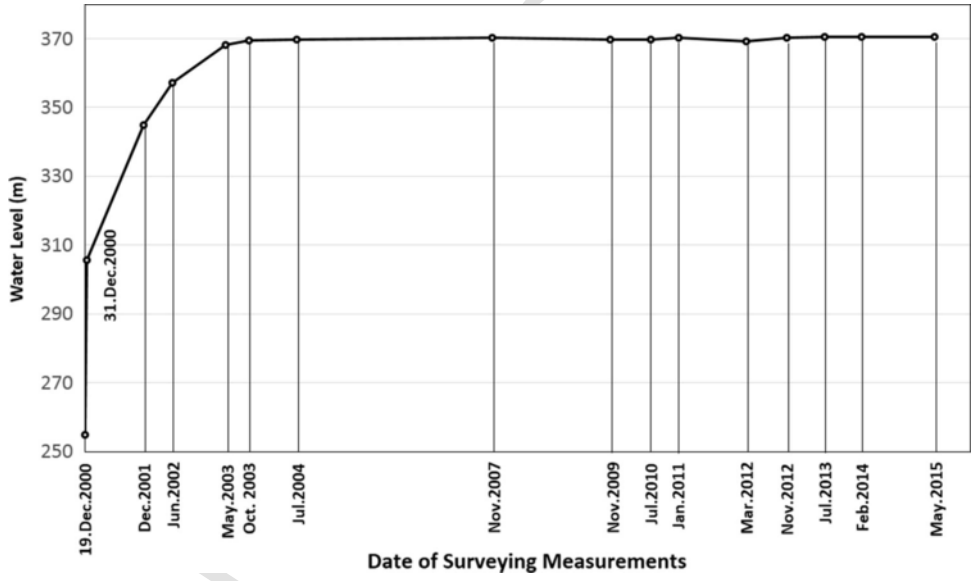

Fig. 3. Water level of the Masjed-Soleyman dam reservoir.

paign in this period included 182 horizontal distance and bearing measurements. With 56 unknown variables, including 50 unknowns for estimating horizontal coordinates of the 25 surveying points and 6 unknowns for estimating zero bearing of the horizontal circles, this results in 126 degrees of freedom for the least-squares adjustment. The maximum Root Mean Square Error (RMSE) values for horizontal and vertical angles were 0.22 and 0.35, respectively.

3.2. InSAR analysis

The SAR data used in this research include 36 X-band images acquired by the German TerraSAR-X mission in SpotLight (SL) mode over the study area: 23 images in descending mode, covering 7 March 2014 to 22 February 2015, and 13 images in ascending mode, covering 24 May 2014 to 10 January 2015. Descending images have

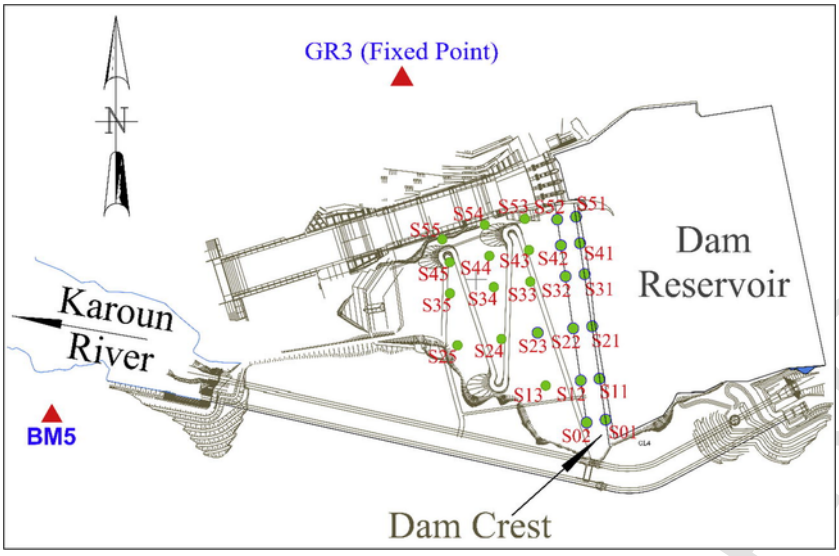

Fig. 4. Location of the geodetic points on the dam. GR3 and BM5 are the fixed points for horizontal and vertical adjustment, respectively.

incidence and heading angles of 36° and 190°, respectively, while ascending images have incidence and heading angles of 35° and 350°, respectively. In SL mode, the TerraSAR-X system uses phased array electrical beam steering in the azimuth direction to increase illumination time and size of the synthetic aperture. This leads to a higher azimuth resolution of approx. 1.5 m at the cost of an azimuth scene size of 10 km by 10 km. Most of the SL data acquired over our study area had a short revisit period of 11 days, except for some gaps in data acquisitions that increased the time interval between images to a maximum 55 days in descending and 88 days in ascending paths.

Data analysis of TerraSAR-X SpotLight data was performed using the Small Baseline Subset [6] time-series approach [17] implemented in StaMPS [32]. For SBAS analysis, we first produced full-resolution differential interferograms from the cropped SAR data (Fig. 5) using the repeat-pass method implemented in DORIS [33]. The linear Doppler frequency shift in azimuth between SpotLight images was accounted for during the interferometric processing following the method proposed by [28]. The six-point cubic convolution kernel was shifted during the resampling step using a Doppler frequency matrix constructed from Doppler information imbedded in the XML metafile [34]. Differential interferograms were then constructed using a 30-m Digital Elevation Model (DEM) for topography-related phase correction and geocoding.

Having made the full-resolution interferograms, we first selected an initial set of candidates, the so-called Persistent Scatterer Candidates (PSCs), using amplitude difference dispersion with a threshold value of 0.6 [16,32]. The interferometric phase of PSCs was further analysed by a statistical analysis of the temporal coherency measure [35], which accounts for the residual phase noise remaining after subtracting both the spatially correlated and spatially uncorrelated contributions to the interferometric phase. Then, coherent pixels were selected that exhibited slow decorrelation over short time intervals, the so-called slowly decorrelating filtered phase (SDFP) pixels. Finally, the wrapped phase of the SDFP pixels was unwrapped using a 3-dimensional phase unwrapping approach [36], and a least-squares inversion was applied to retrieve the displacement time-series. For simplicity, we refer to SDFT pixels as coherent pixels.

Because of the low sensitivity of the ascending interferogram to dam deformation (further discussed in Section 4.2), time-series analysis using the SBAS method was performed on only descending data. Fig. 6 illustrates the temporal-spatial baseline distribution of the final interferometric pairs used for time-series analysis; the circles represent acquisition dates, while the lines connecting the circles represent interferograms. As shown in Fig. 6, the network was fully connected, so the design matrix had a full rank, and no regularization was needed for the inversion [17].

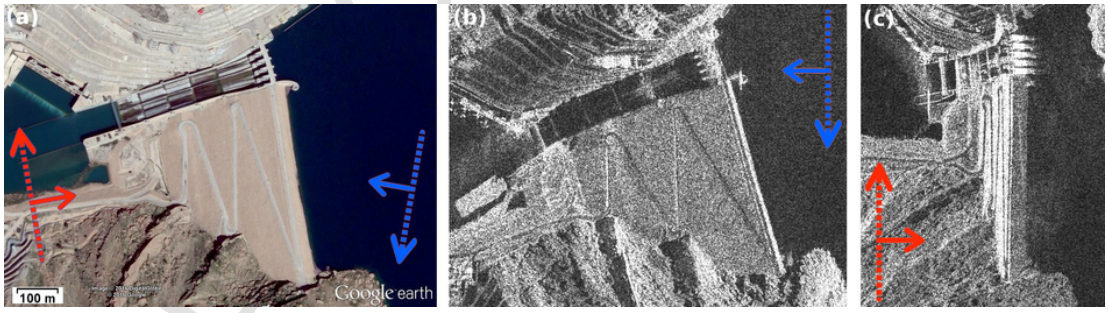

Fig. 5. (a) Google Earth™ image of the study area: dashed arrows and solid arrows represent the heading and LOS direction, respectively; red arrows correspond to the ascending track and the blue to the descending track. (b) and (c) illustrate the amplitude of cropped TSX images over our study area in descending and ascending orbits, respectively. (For interpretation of the references to colour in this figure legend, the reader is referred to the web version of this article.)

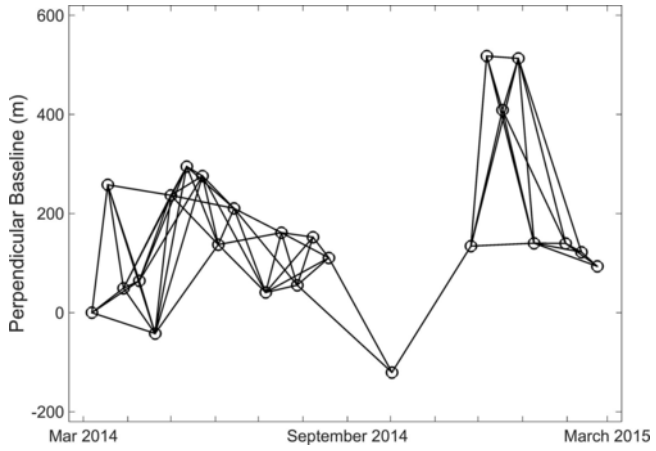

Fig. 6. Network of interferograms in SBAS method for descending images.

4. Results

4.1. Surveying measurements

Fig. 7 shows the temporal progression of horizontal and vertical surface displacement at Masjed-Soleyman dam for the time period 2000–2015. For a better visualization, surveying measurements are linearly interpolated. Surveying measurements suggest that for the time period 2000–2015 significant cumulative subsidence of more than 3 m occurred at both the eastern edge (control points S21 and S31) and the western edge (control points S22 and S32) of the crest. Maximum settlement is concentrated on the crest, and it gradually decreases as we move downward along the downstream embankments. The pattern of surface deformation also contains horizontal motion. The downstream body of the dam primarily shows significant horizontal motion, with a 1.4 m maximum occurring between December 2000 to May 2015. The cumulative horizontal displacements at the crest are smaller than the ones at downstream, with a maximum cumulative horizontal motion of about 90 cm occurring between 2000 and 2015 for the point S41 on the crest near the spillway. Interestingly, on both sides of the crest we see an additional component in the horizontal motion along the axis of the dam. From the plot in Fig. 7, we infer that between 2000 and 2015 the amount of cumulative vertical settlement was approximately 3 times larger than the horizontal motion.

As previously explained in Section 3, for comparison with InSAR observations (Section 5.1), we only used part of the results illustrated in Fig. 7, corresponding to the 2014–2015 time period, which overlap with the InSAR data. Table 1 lists the results corresponding to this surveying campaign. The maximum error, the semi-major axis of error ellipse, for the estimated horizontal coordinates is 2.9 mm, corresponding to point S54. The maximum estimated height error is < 1.5 mm .

4.2. SBAS interferograms

Figs. 8 and 9 show examples of descending and ascending interferograms processed from TerraSAR-X SpotLight data, respectively. The displacement fringes are clearly visible in the descending interferograms. This results from the geometry of the downstream slope, which is favourable for the descending data used in this study. With an incidence angle of $\theta = 36°$ for descending TSX SAR images and a slope angle of $\alpha = 30°$, the amount of foreshortening for a distance l on the downstream slope (back slope for descending geometry) would be equal to $l \sin(\theta + \alpha) = 0.9l$ [37]. As a result, the downstream slope does not suffer significantly from foreshortening in descending acquisitions, also clearly visible in Fig. 5, resulting in favourable interferometry measurements. As shown in Fig. 8, descending X-band interferograms suggest that the dam is subject to two completely separate deformation regimes. One is related to downstream embankments, where we see concentric circular fringes, the number of which increases with the temporal baseline. The second (red rectangle in Fig. 8c) is related to the dam's crest (black dashed line) and its immediate neighbouring area downstream and upstream. The boundary between the two regions is clearly visible in interferograms with short temporal baselines (Fig. 8b, c), but difficult to follow in interferograms with large temporal baselines (>209 days) due to temporal decorrelation on the crest area.

In contrast to the descending interferograms, the ascending interferograms show squeezed fringes on the downstream slope of the dam. This results from the geometry of the downstream slope, which is close to perpendicular to the Line-Of-Sight (LOS) direction of ascending images, leading to significant foreshortening of the SAR images. Considering the incidence angle of $\theta = 35°$ of the ascending TSX SAR images and the slope angle of $\alpha = 30°$, the amount of foreshortening for a distance l on the downstream slope (fore slope for ascending geometry) is equal to $l \sin(\theta - \alpha) = 0.08l$. The effect of such significant foreshortening is also clearly visible in the amplitude image in Fig. 5c, where slope details are lost, and the amplitude image looks very bright. As a result, displacement fringes on the downslope embankment will not properly appear in the ascending interferograms of Fig. 9.

4.3. InSAR time-series

Fig. 10a illustrates the average 2014–2015 LOS velocity map for the dam area obtained using the network constructed in Fig. 6. Fig. 10b corresponds to standard deviation of the mean LOS velocity. The SBAS analysis of TSX SpotLight data provides more than 65,000 coherent pixels for displacement measurements on the dam, corresponding to a density of 1 measurement point per 2 m^2 area. The velocity map clearly indicates that the dam area is subject to two spatially variable deformation regimes: one on the crest and the other on the downstream slope. The deformation patterns in these two regions separate from each other on the upper part of the downstream section. Most of the estimated mean velocities have standard deviations less than 4 mm/yr, but there are areas where the standard deviations reach up to 1 cm/yr. This is caused either by unwrapping errors, e.g. in slopes outside the downslope embankment due to foreshortening, or deviation of deformation rate in these areas being greater than the mean velocity that assumes linear deformation.

Maximum settlement occurs on the crest and its adjacent area downstream (marked by 1 in Fig. 10a), where LOS velocity amounts to approximately 13 cm/yr for the 2014–2015 period. The maximum LOS velocity on the lower part of the downstream reaches approximately 7 cm/yr for 2014 to 2015.

5. Discussion

Fig. 11 illustrates the time-series of InSAR-derived displacement close to the location of geodetic points on the dam. As shown, except for points S51 to S55, which are close to the spillway (Fig. 4), and those points located at the bottom part of the downstream section (S45, S35, S25), the remaining locations on the crest and downstream do not show signs of temporal stability at almost 15 years after com-

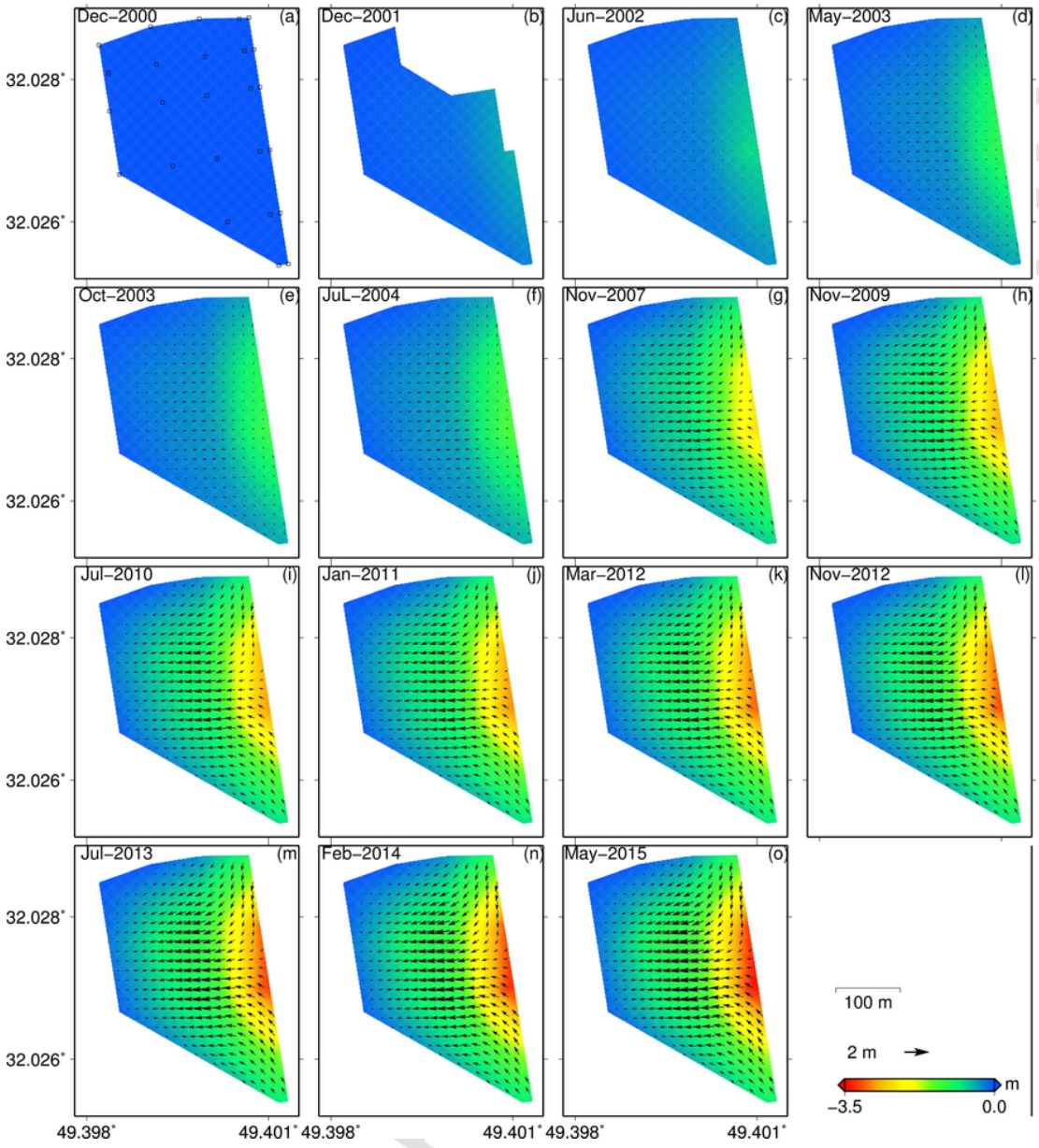

Fig. 7. (a)–(o) The progression of horizontal and vertical displacement at Masjed-Soleyman dam, inferred from terrestrial surveying measurements for the time period 2000–2015. The displacement values are with respect to the first time period of terrestrial measurements in December 2000. The arrows show horizontal motion, while the background colour illustrates the vertical displacement. Black squares represent the geodetic points (Fig. 4). The zigzag pattern in Fig. 7b reflects an incomplete survey of the points measured in December 2001. (For interpretation of the references to colour in this figure legend, the reader is referred to the web version of this article.)

pletion of the dam. In particular, points that sustained maximum settlement (e.g., S31-S33 and S21-24) show a clear declining trend in LOS displacement. To better visualize the spatial pattern of deformation, we extracted velocity profiles at five cross sections along the axis of the crest that cross the geodetic points and plotted them in Fig. 12. As shown in Fig. 12, except for the last profile, which is located on the lowest part of the downstream section, the displacement pattern at all other profiles show a clear concave pattern, resulting from the dam settling. The amount of subsidence increases from the outer border of the dam to the middle. This is in general in agreement with the estimation provided by geodetic measurements, suggesting that the rate of settlement has not stabilized in major parts of the Masjed-Soleyman dam.

5.1. Comparison with geodetic measurements

For quality assessment of InSAR results, we compared them with the ground-based measurements at surveying points for the period 2014–2015. As the surveying measurements provide information for both horizontal and vertical displacements, we first projected them to the LOS direction using the following relation [38]:

$$d^{c}_{los} = d_u \cos(\theta) - \left[d_n \cos(\gamma - 3\pi/2) + d_e \sin(\gamma - 3\pi/2)\right] \sin(\theta$$

where γ is the azimuth of the satellite's track, θ is the incidence angle of the radar wave, and d_e, d_n and d_u are 3 components of displacement in east-west, north-south and vertical directions, respectively,

Table 1
Horizontal (ΔX & ΔY) and vertical (Dz) displacement corresponding to the 2014–2015 surveying campaign. A and B represent semi-major and semi-minor axes of the error ellipse, respectively, at 95% confidence interval, and az is the azimuth of the major axis of the ellipse. MDz is the standard deviation of vertical displacement.

Point Name	ΔX (mm)	ΔY (mm)	A (mm)	B (mm)	az (deg)	Dz (mm)	MDz (mm)
S01	−15.28	15.56	1.5	0.8	120	−24.63	1.3
S02	−15.25	19.78	2	1.8	179	−25.63	1.3
S11	−20.29	39.12	2	1.4	141	−78.26	1.3
S12	−19.72	36.19	2	1.8	166	−70.5	1.3
S13	−26.07	10.28	1.9	1.8	169	−26.55	1.3
S21	−37.25	16.52	1.7	1.5	148	−165.2	1.3
S22	−40.03	12.03	1.6	1.5	145	−151.93	1.3
S23	−71.81	−11.69	2.6	1.8	150	−72.16	1.2
S24	−29.04	−1.86	2.2	1.7	148	−32.98	1.1
S25	−3.64	−1.54	1.9	1.6	153	−2.74	0.9
S31	−2.28	−35.6	1.8	1.6	121	−144.65	1.3
S32	2.12	−35.98	2.2	2	129	−114.22	1.3
S33	−61.13	−17.93	2	1.8	136	−60.43	1.2
S34	−26.63	−12.3	2.1	1.8	111	−39.34	1.1
S35	−2.86	−3.79	2.1	1.7	139	−5.39	0.9
S41	1.8	−45.92	2.3	2	69	−80.24	1.4
S42	1.2	−41.69	2	1.6	140	−65.84	1.4
S43	−30.21	−20.2	2	1.7	134	−29.89	1.2
S44	−13.47	−11.39	2.7	2	133	−14.93	1.1
S45	−1.03	−3.08	2.5	2	129	−2.94	1
S51	4.52	−29.84	1.8	1.5	120	−48.21	1.4
S52	1.64	−30.29	2	1.5	137	−34.21	1.4
S53	−4.65	−8.36	2	1.5	137	−5.13	1.2
S54	1.14	−3.35	2.9	2.1	128	0.8	1.2
S55	0.2	−0.72	2.6	2	124	−0.32	1

measured by terrestrial surveying. The velocity is then obtained by scaling the computed LOS motion, d^c_{los}, according to the time interval of the last time period (14.5 months).

The scatter diagram plotted in Fig. 13 illustrates correlation coefficients between InSAR and geodetic results at surveying points; the squares and triangles correspond to the points on the crest and body, respectively. We computed correlation coefficients using least-squares regression for three scenarios: (1) points located on the crest (squares in Fig. 13), (2) points located downstream (triangles in Fig. 13), and (3) all the points together.

As shown in Fig. 13, the correlation coefficient between terrestrial geodetic and InSAR measurements at all points (solid line in Fig. 13) is 0.97. The correlation for points on the crest (dashed line in Fig. 13) is 0.95, while for points on the body it is slightly (4%) higher, i.e., 0.99 (dot-dashed line). The lower correlation for points on the crest in comparison to points downstream can be related to the relatively large deformation at the crest. This leads to large fringe gradient in a relatively short distance, 15 m crest width, especially for interferograms with large temporal baselines, in turn causing phase unwrapping problems and underestimation of deformation using InSAR.

5.2. The importance of InSAR surveys

The InSAR time-series analysis provides spatially dense measurements of surface deformations on the crest and downstream embankment, enabling us to assess the complete pattern of structure stability that is difficult to obtain precisely using sparse ground-based geodetic measurements. To better illustrate this point, we evaluated the difference between interpolated velocity map from geodetic measurements and the velocity obtained using InSAR analysis for the 2014–2015 time period. The geodetic velocity map (Fig. 14a) was obtained by interpolating the geodetic measurement using linear polynomials to derive the pattern of deformation everywhere on the dam. To be comparable with InSAR, horizontal and vertical displacements from geodetic measurements were projected into LOS (Fig. 14b). The residual map in Fig. 14d was then derived by subtracting this map from the InSAR observations in Fig. 14c. The negative sign in Fig. 14d corresponds to underestimation by InSAR and vice versa.

As shown in Fig. 14d, in neighbouring geodetic points, we observe very good consistency between InSAR and interpolated geodetic maps, except for points on the upstream edge of the crest, where

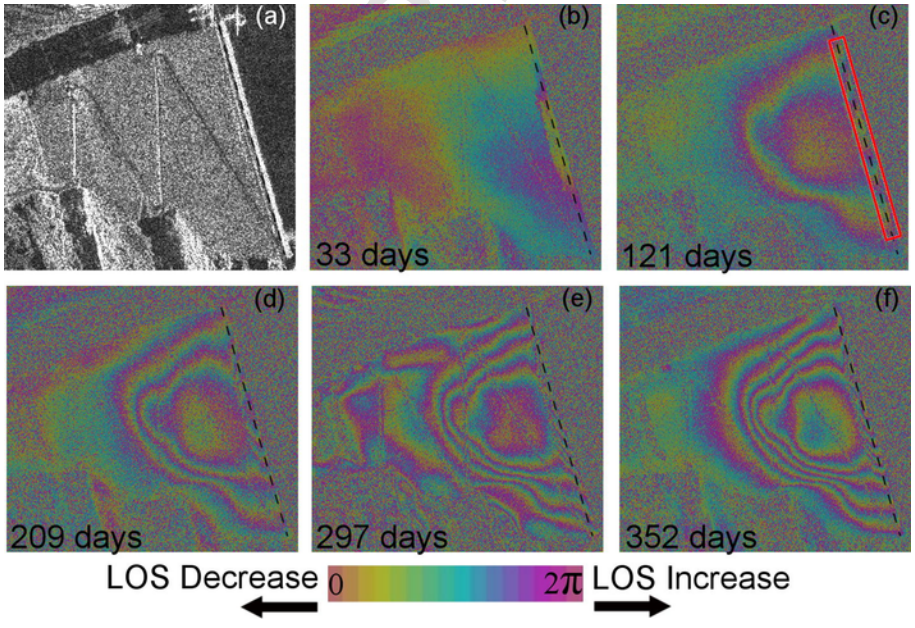

Fig. 8. Descending TSX interferograms. (a) Amplitude of SAR image. (b-f) Differential interferograms showing progressive displacement relative to the reference master date on 7 March 2014. One full colour cycle corresponds to 3.1 cm of LOS motion. Red rectangle delineates deformation area related to the crest, marked with dashed black line, and its adjacent area downstream. (For interpretation of the references to colour in this figure legend, the reader is referred to the web version of this article.)

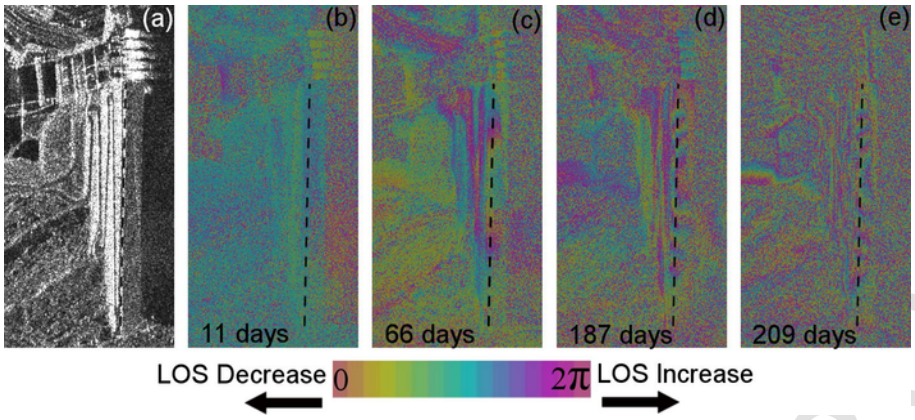

Fig. 9. Ascending TSX interferograms. (a) Amplitude of SAR image. (b-e) Differential interferograms showing progressive displacement relative to the master date on 24 May 2014. One full colour cycle corresponds to 3.1 cm of LOS motion. The dashed black line indicates the crest of the dam. (For interpretation of the references to colour in this figure legend, the reader is referred to the web version of this article.)

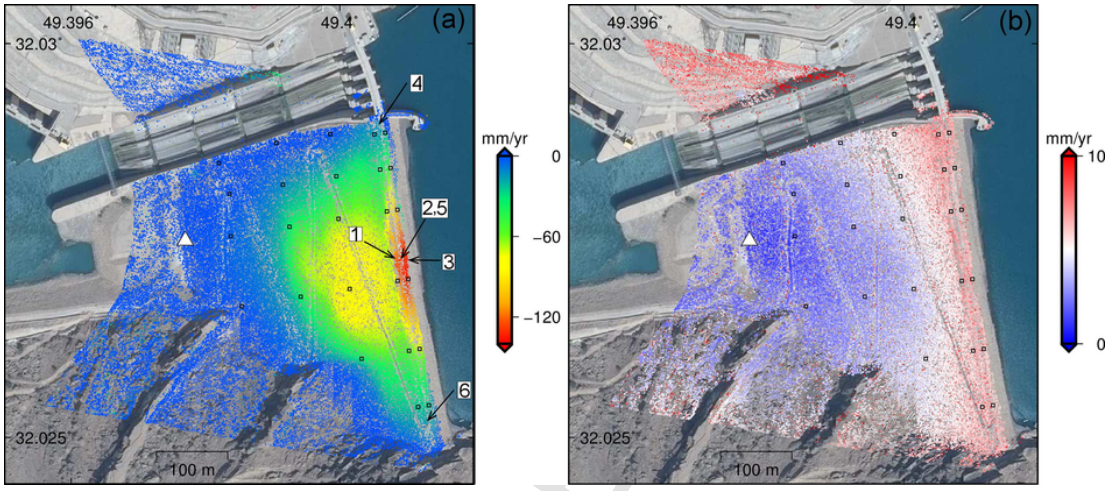

Fig. 10. (a) Average 2014–2015 displacement rate along the LOS direction derived from TSX SpotLight data overlaid on a Google Earth™ image. The white triangle is the location of the InSAR measurement reference point. The black squares are locations of geodetic points (See Fig. 4 for names). The numbers (1–6) correspond to locations of ground pictures illustrated in Fig. 16. (b) Standard deviations of mean LOS velocity.

InSAR underestimates deformation, as discussed previously. However, between geodetic points, large residuals of up to 3 cm/yr are observed in the middle of the downstream embankment due to the poor density of geodetic monuments. Such observations have important implications for reliably assessing the long-term settlement behaviour of dams using mechanical and numerical models in which the results at the surveying points are interpolated to determine nodal values for a particular element [8]. The temporal and spatial characteristics of surface deformation obtained from analysis of high-resolution TSX SAR data can significantly improve dynamic numerical models constrained by such surface boundary conditions [20].

5.3. The importance of full-resolution SBAS analysis

The small spatial scale of surface deformation at the crest of the dam requires pixel-wise SBAS time-series analysis and interferometric processing. The cross-track (range) resolution of TerraSAR-X data in SpotLight acquisition is 2.01 m in slant range, equivalent to 3.4 m on the ground, considering the incidence angle of 35.73° for the dataset. Along-track (azimuth) resolution is slightly higher, approximately 1.6 m on the ground.

The standard SBAS approach proposed in [17,39–41] uses multi-looked interferograms for time-series analysis. For crest monitoring, although these multi-looking factors might decrease noise artefacts in differential interferograms and improve the efficiency of phase unwrapping, they can also be problematic. Fig. 15 shows the effect of two exemplary multi-looking factors of five and ten on two interferograms with temporal baselines of 33 days (Fig. 15b) and 352 days (Fig. 15c); the multi-looking factor of 5 corresponds to approximately 8 × 17 m rectangular pixels, and 10 corresponds to 16 × 34 m rectangular pixels.

As shown in Fig. 15, the best displacement fringes are observed when we process the interferograms at full resolution (Fig. 15b-c). The fringe visibility of the crest area is best observed in the full-resolution 33-day interferogram, but is lost in interferograms with long-temporal baselines using a multi-looking factor of 5 (Fig. 15f). For the multi-looking factor of 10, the fringe visibility in crest area is lost in both short-term and long-term interferograms (Fig. 15h-i). This loss is related to the proximity of pixels at the dam's crest with noisy pixels from the upstream region (water reservoir). When these pixels are combined together using a multi-looking factor of 10, the details are lost, and no reliable information for the crest could be exploited from the differential interferometry analysis. For the down-

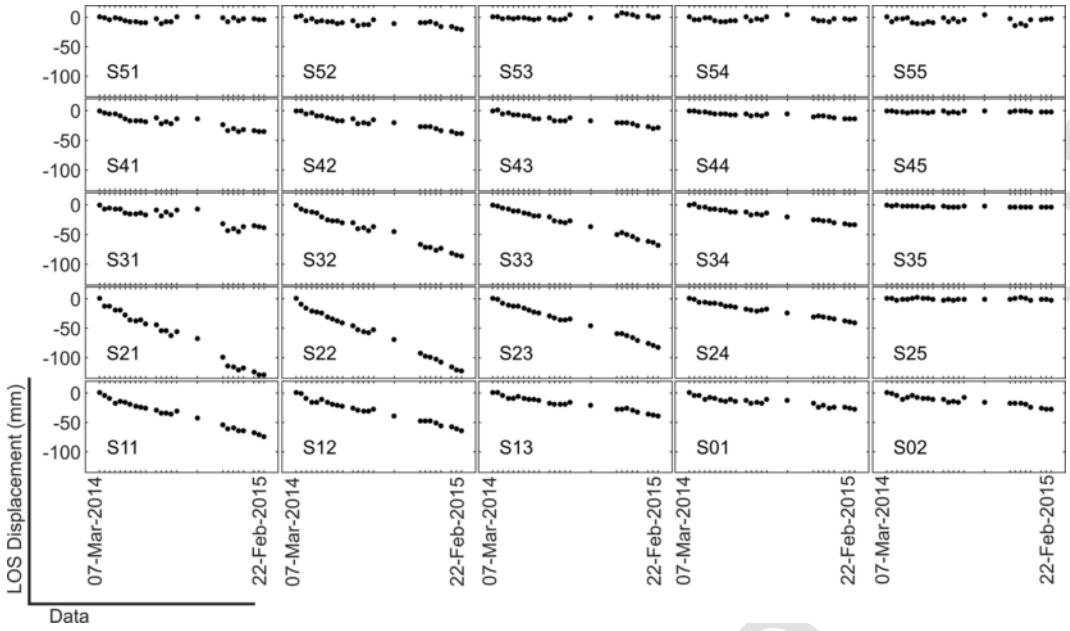

Fig. 11. LOS time series of geodetic network points located on the dam crest and downstream embankment derived from InSAR processing of high resolution TSX images.

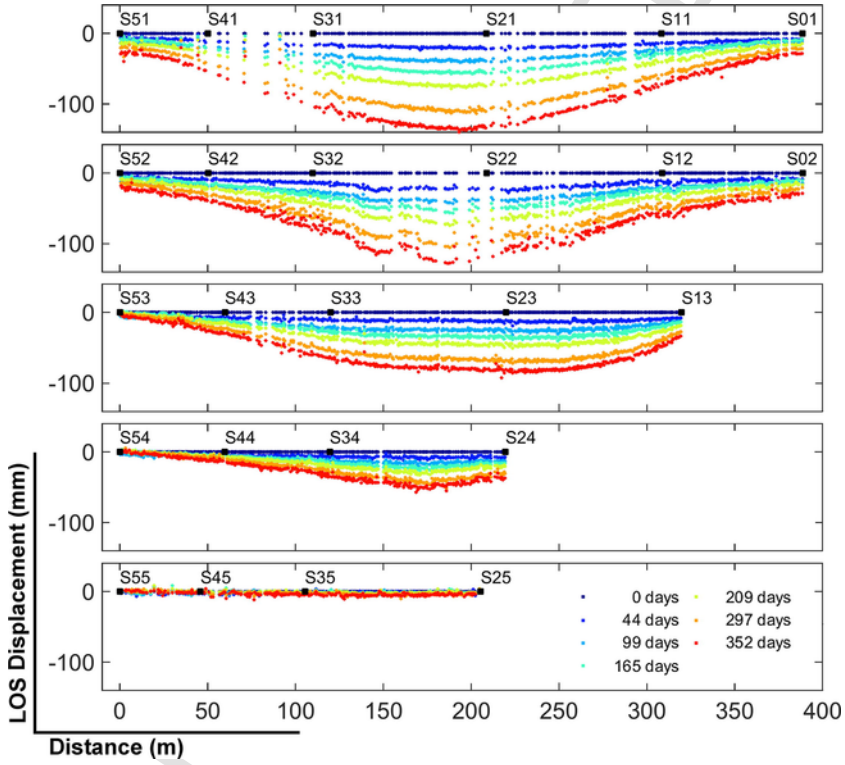

Fig. 12. Profile of LOS displacement for different time intervals inferred from InSAR at terrestrial geodetic network locations. Displacements are with respect to the date 7 March 2014.

stream area, the details of surface deformation are clearly visible in the full-resolution 352-day interferogram, but are reduced to some extent with the multi-looking factor of 5 (Fig. 15e-f). Applying a uniform multi-looking factor of 10 greatly affects the quality of the information extracted for the down-stream area from differential interferograms (Fig. 15h-i). This illustrates the importance of performing point-wise InSAR techniques [16,42,43] and/or selecting adaptive [44] and realistic multi-looking factors [45] for investigating local and small scale deformation signals in engineering structures. It is worth noting that the SBAS analysis implemented in StaMPS works based on single-look images to identify single-look coherent pixels. Therefore, interferograms are processed at the highest possible resolution, enabling identification of isolated coherent pixels on the crest that are surrounded by decorrelated pixels upstream. Therefore,

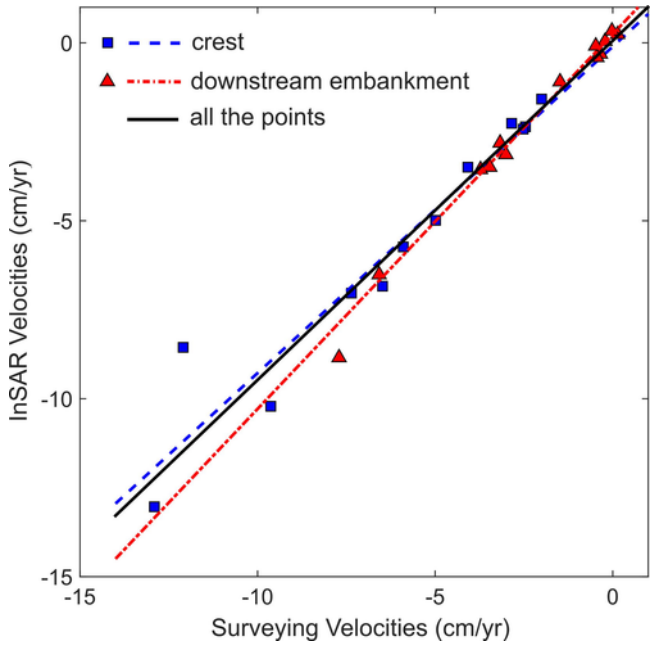

Fig. 13. Correlation analysis of InSAR and geodetic measurements. Squares and triangles represent points on the crest and downstream embankment, respectively. The dashed line, dot-dashed line and solid line are the correlations for the crest, body, and all points, respectively.

StaMPS can detect enough coherent pixels for deformation analysis over the width of the crest, as already illustrated in the velocity map in Fig. 10.

5.4. Field survey

The study area was visited in March 2016 to find evidence of damage derived from deformation of the dam as detected by both ISAR and geodetic observations. Fig. 16 illustrates examples of dislocation cracks in different parts of the dam documented by this fieldwork. Both the crest and upstream and downstream embankments sustained visible damage and settling. Fig. 16a and c illustrate distortion on the upper part of the downstream and upstream embankments, respectively, which were caused by differential subsidence in that region. Major fractures had developed at the junction of concrete or steel elements to the shell of the rockfill dam (e.g., Fig. 16d, e), damaging the asphalt and guardrails. Minor damage, composed mainly of longitudinal cracks, was also detected on the road surface on the dam crest (Fig. 16f). All pieces of field evidence presented in Fig. 16 reflect inelastic deformation behaviour caused by long-term consolidation processes in the crest foundation and embankments.

6. Conclusion

Due to high-spatial resolution and a relatively short revisit time, the interferometric analysis of X-band SpotLight SAR images provides a very detailed stability assessment of embankment dams and engineering structures in both space and time. It is worth noting that the outcome of high-resolution interferometry analysis depends on data availability. The pre-existing high-resolution SAR sensors aboard the TerraSAR-X do not have an extensive background acquisition program for the continuous monitoring of a particular engineering structure such as dams and buildings at risk. The acquisitions need to be programmed based on request, which sometimes leads to conflicts with other requests for military, industrial and commercial use. The conflict creates a temporal gap in the data stack due to failure of one or even several acquisitions, causing phase unwrapping errors in areas subject to large deformation gradients. Moreover, slope geometry of the embankments and geometrical distortions induced by side-looking acquisition geometry of SAR systems can limit the applicability of high-resolution InSAR measurements for detailed, local scale monitoring. For east-facing and west-facing embankments, useful SAR signals can be obtained for cases where the incidence angle is equal to or greater than the slope angle. Otherwise, the shadowing or layover effect renders the SAR signal useless.

At the Masjed-Soleyman rockfill dam, SpotLight interferometry analysis with TerraSAR-X SAR data reveals significant displacements on the crest and downstream slope. The maximum displacement rate at the crest reaches approximately 13 cm/yr along the satellite line of sight, corresponding to approximately 15 cm/yr by ignoring horizontal motion. Total settling of rockfill structures is expected to complete 24–30 months following the end of construction, when the settlement rate is less than 0.02% of the crest height [1]. Therefore, we can conclude that instability process is still affecting the Masjed-Soleyman dam, which after 15 years of construction shows a settlement rate of approximately 0.08% of its height. Future research should focus on using this valuable result to design a better ground-based surveying network that can capture the strain field more precisely at a higher spatial resolution. This will play a key role in developing reliable dynamic and numerical models of stability using finite element methods for dam safety analysis and the mitigation of associated hazards.

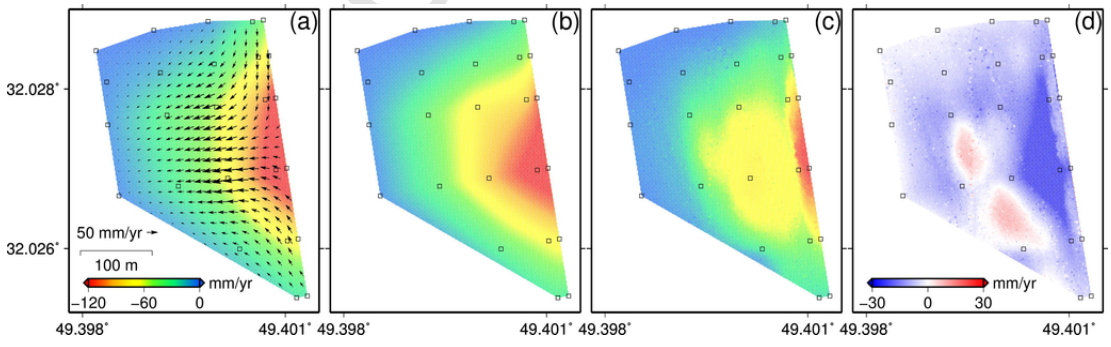

Fig. 14. (a) Horizontal and vertical map from the last period of geodetic observations. The background colour shows the vertical deformation rate, and the arrows show horizontal displacement. (b) Interpolated LOS observation from geodetic measurements. (c) InSAR LOS velocity map. (d) Residual after subtracting (b) from (c).

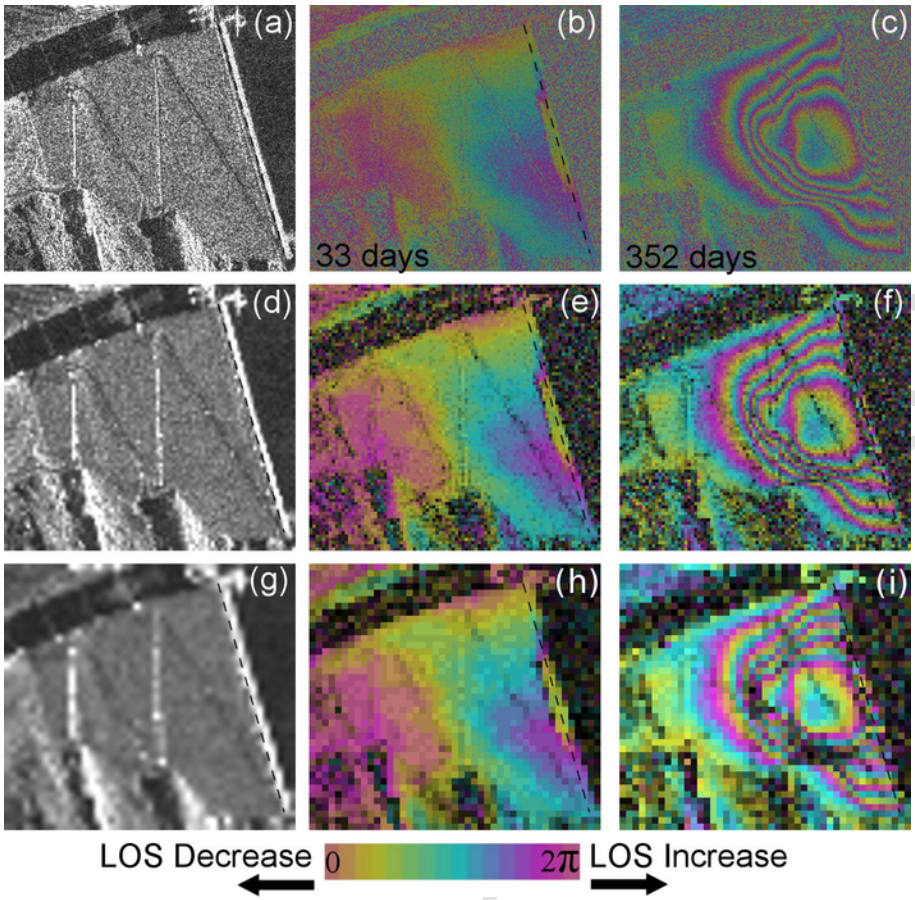

Fig. 15. The effect of multi-looking. The images on the top row include (a) amplitude, (b) 33-days and (c) 352-days interferograms from a descending orbit in full-resolution. The amplitude and interferograms in the middle row and bottom row correspond to those illustrated in the upper row, but with multi-looking factors of 5 (d–f) and 10 (g–i), respectively. One full colour cycle corresponds to 3.1 cm of LOS motion.

Acknowledgements

This work was supported by the Initiative and Networking Fund of the Helmholtz Association in the frame of the Helmholtz Alliance's "Remote Sensing and Earth System Dynamics". TerraSAR-X original data is copyright German Aerospace Agency (DLR) and provided under proposal motagh_GEO1916. We would like to thank the journal Editor, Dr. Herbert Mang, and 3 anonymous reviewers fro their very helpful and insightful comments, which greatly improved the quality of the original manuscript.

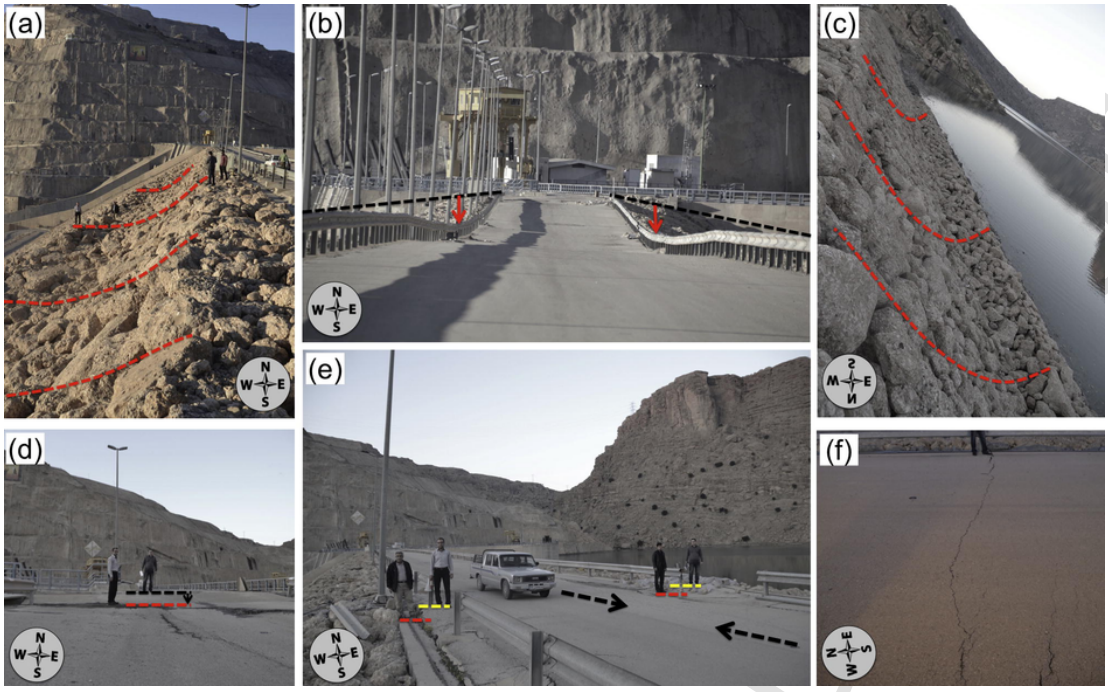

Fig. 16. Examples of observed damage on the crest and embankments. (a)-(f) correspond to locations marked by 1–6 in Fig.10a. (a) Localized subsidence on the downstream embankment. (b) Subsidence on the road surface on the crest. (c) Localized subsidence on the upstream embankment. (d, e) Two dislocation fractures at the border of the crest. (f) Minor crack on the road pavement of the crest.

References

[1] O. Dascal, Postconstruction deformations of rockfill dams, J Geotech Eng 113 (1987) 46–59.
[2] R.P. Clements, Post-construction deformation of rockfill dams, J Geotech Eng 110 (1984) 821–840.
[3] A. Szostak-Chrzanowski, A. Chrzanowski, M. Massiéra, Use of deformation monitoring results in solving geomechanical problems—case studies, Eng Geol 79 (2005) 3–12.
[4] Hunter G, Fell R. The deformation behaviour of embankment dams: University of New South Wales, School of Civil and Environmental Engineering; 2003.
[5] S.I. Pytharouli, S.C. Stiros, Ladon dam (Greece) deformation and reservoir level fluctuations: evidence for a causative relationship from the spectral analysis of a geodetic monitoring record, Eng Struct 27 (2005) 361–370.
[6] G. Guler, H. Kilic, G. Hosbas, K. Ozaydin, Evaluation of the movements of the dam embankments by means of geodetic and geotechnical methods, J Surv Eng 132 (2006) 31–39.
[7] Y. Kalkan, Geodetic deformation monitoring of Ataturk Dam in Turkey, Arab J Geosci 7 (2012) 397–405.
[8] V. Gikas, M. Sakellariou, Settlement analysis of the Mornos earth dam (Greece): evidence from numerical modeling and geodetic monitoring, Eng Struct 30 (2008) 3074–3081.
[9] R.B. Jansen, Advanced dam engineering for design, construction, and rehabilitation, Springer Sci Business Media (2012).
[10] M. Stewart, M. Tsakiri, The application of GPS to dam surface monitoring, J Geospatial Eng 3 (2001) 45–58.
[11] M. Motagh, T.R. Walter, M.A. Sharifi, E. Fielding, A. Schenk Anderssohn, J. Zschau, Land subsidence in Iran caused by widespread water reservoir overexploitation, Geophys Res Lett 35 (2008) L16403, http://dx.doi.org/10.1029/2008GL033814.
[12] M. Motagh, W. Hans-Ulrich, R. Sigrid, K. Hermann, A TerraSAR-X InSAR study of landslides in southern Kyrgyzstan, Central Asia, Remote Sens Lett 4 (2013) 657–666.
[13] M. Motagh, B. Schurr, J. Anderssohn, B. Cailleau, T.R. Walter, R. Wang, et al., Subduction earthquake deformation associated with 14 November 2007, Mw 7.8 Tocopilla earthquake in Chile: Results from InSAR and aftershocks, Tectonophysics 490 (2010) 60–68.
[14] C. Colesanti, J. Wasowski, Investigating landslides with space-borne Synthetic Aperture Radar (SAR) interferometry, Eng Geol 88 (2006) 173–199.
[15] M. Motagh, R. Shamshiri, M. Haghshenas Haghighi, H.-U. Wetzel, B. Akbari, H. Nahavandchi, et al., Quantifying groundwater exploitation induced subsidence in the Rafsanjan plain, southeastern Iran, using InSAR time-series and in situ measurements, Eng Geol 218 (2017) 134–151.
[16] A. Ferretti, C. Prati, F. Rocca, Permanent scatterers in SAR interferometry, IEEE Trans Geosci Remote Sens 39 (2001) 8–20.
[17] P. Berardino, G. Fornaro, R. Lanari, E. Sansosti, A new algorithm for surface deformation monitoring based on small baseline differential SAR interferograms, IEEE Trans Geosci Remote Sens 40 (2002) 2375–2383.
[18] A. Sowter, L. Bateson, P. Strange, K. Ambrose, M.F. Syafiudin, DInSAR estimation of land motion using intermittent coherence with application to the South Derbyshire and Leicestershire coalfields, Remote Sens Lett 4 (2013) 979–987.
[19] S. Vajedian, M. Motagh, F. Nilfouroushan, StaMPS improvement for deformation analysis in mountainous regions: implications for the Damavand Volcano and Mosha Fault in Alborz, Remote Sens 7 (2015) 8323.
[20] R. Shamshiri, M. Motagh, M. Baes, M. Sharifi, Deformation analysis of the Lake Urmia causeway (LUC) embankments in northwest Iran: insights from multi-sensor interferometry synthetic aperture radar (InSAR) data and finite element modeling (FEM), J Geodesy 88 (2014) 1171–1185.
[21] G. Herrera, F. Gutiérrez, J.C. García-Davalillo, J. Guerrero, D. Notti, J.P. Galve, et al., Multi-sensor advanced DInSAR monitoring of very slow landslides: The Tena Valley case study (Central Spanish Pyrenees), Remote Sens Environ 128 (2013) 31–43.
[22] M. Crosetto, O. Monserrat, M. Cuevas-González, N. Devanthéry, B. Crippa, Persistent Scatterer Interferometry: a review, ISPRS J Photogr Remote Sens 115 (2016) 78–89.
[23] R. Tomás, M. Cano, J. García-Barba, F. Vicente, G. Herrera, J.M. Lopez-Sanchez, et al., Monitoring an earthfill dam using differential SAR interferometry: La Pedrera dam, Alicante, Spain, Eng Geol 157 (2013) 21–32.
[24] P. Milillo, D. Perissin, J.T. Salzer, P. Lundgren, G. Lacava, G. Milillo, et al., Monitoring dam structural health from space: Insights from novel InSAR techniques and multi-parametric modeling applied to the Pertusillo dam Basilicata, Italy, Int J Appl Earth Obs Geoinf 52 (2016) 221–229.
[25] M. Haghshenas Haghighi, M. Motagh, Assessment of ground surface displacement in Taihape landslide, New Zealand, with C-and X-band SAR interferometry, NZ J Geol Geophys 59 (2016) 136–146.
[26] F. Bovenga, J. Wasowski, D.O. Nitti, R. Nutricato, M.T. Chiaradia, Using COSMO/SkyMed X-band and ENVISAT C-band SAR interferometry for landslides analysis, Remote Sens Environ 119 (2012) 272–285.
[27] J. Wasowski, F. Bovenga, Investigating landslides and unstable slopes with satellite Multi Temporal Interferometry: current issues and future perspectives, Eng Geol 174 (2014) 103–138.

[28] M. Eineder, N. Adam, R. Bamler, N. Yague-Martinez, H. Breit, Spaceborne spotlight SAR interferometry with TerraSAR-X, IEEE Trans Geosci Remote Sens 47 (2009) 1524–1535.
[29] Gernhardt S, Bamler R. Towards Deformation Monitoring of Single Buildings - Persistent Scatterer Interferometry using TerraSAR-X Very High Resolution Spotlight Data. 8th European Conference on Synthetic Aperture Radar 2010. p. 1–4.
[30] R. Bamler, M. Eineder, N. Adam, X. Zhu, S. Gernhardt, Interferometric potential of high resolution spaceborne SAR, Photogrammetrie – Fernerkundung – Geoinform 2009 (2009) 407–419.
[31] P. Vanicek, E.J. Krakiwsky, Geodesy: the concepts, Elsevier, 2015.
[32] A. Hooper, A multi-temporal InSAR method incorporating both persistent scatterer and small baseline approaches, Geophys Res Lett 35 (2008) http://dx.doi.org/10.1029/2008GL034654.
[33] Kampes B, Hanssen R, Perski Z. Radar Interferometry with Public Domain Tools. Fringe 2003, Available online at: http://earthesaint/fringe03/ proceedings/papers/22_kampespdf (accessed 21 July 2016)2003.
[34] M. Jendryke, T. Balz, H. Jiang, M. Liao, U. Stilla, Using open-source components to process interferometric TerraSAR-X spotlight data, Int J Antennas Propag 2013 (2013), 275635.
[35] A. Hooper, H. Zebker, P. Segall, B. Kampes, A new method for measuring deformation on volcanoes and other natural terrains using InSAR persistent scatterers, Geophys Res Lett 31 (2004) http://dx.doi.org/10.1029/2004GL021737.
[36] A. Hooper, H.A. Zebker, Phase unwrapping in three dimensions with application to InSAR time series, J Opt Soc Am A: 24 (2007) 2737–2747.
[37] F. Cigna, L.B. Bateson, C.J. Jordan, C. Dashwood, Simulating SAR geometric distortions and predicting Persistent Scatterer densities for ERS-1/2 and ENVISAT C-band SAR and InSAR applications: Nationwide feasibility assessment to monitor the landmass of Great Britain with SAR imagery, Remote Sens Environ 152 (2014) 441–466.
[38] R.F. Hanssen, Radar interferometry: data interpretation and error analysis, Springer, Netherlands, 2001.
[39] J. Anderssohn, M. Motagh, T.R. Walter, M. Rosenau, H. Kaufmann, O. Oncken, Surface deformation time series and source modeling for a volcanic complex system based on satellite wide swath and image mode interferometry: The Lazufre system, central Andes, Remote Sens Environ 113 (2009) 2062–2075.
[40] D.A. Schmidt, R. Bürgmann, Time-dependent land uplift and subsidence in the Santa Clara valley, California, from a large interferometric synthetic aperture radar data set, J Geophys Res 108 (2003) http://dx.doi.org/10.1029/2002JB002267.
[41] V. Akbari, M. Motagh, Improved ground subsidence monitoring using small baseline SAR interferograms and a weighted least squares inversion algorithm, Geosci Remote Sens Lett IEEE 9 (2012) 437–441.
[42] A. Ferretti, A. Fumagalli, F. Novali, C. Prati, F. Rocca, A. Rucci, A new algorithm for processing interferometric data-stacks: SqueeSAR, IEEE Trans Geosci Remote Sens 49 (2011) 3460–3470.
[43] P. Shanker, H. Zebker, Persistent scatterer selection using maximum likelihood estimation, Geophys Res Lett 34 (2007) http://dx.doi.org/10.1029/2007GL030806.
[44] A. Parizzi, R. Brcic, Adaptive InSAR stack multilooking exploiting amplitude statistics: a comparison between different techniques and practical results, IEEE Geosci Remote Sens Lett 8 (2011) 441–445.
[45] R. Lanari, O. Mora, M. Manunta, J.J. Mallorqui, P. Berardino, E. Sansosti, A small-baseline approach for investigating deformations on full-resolution differential SAR interferograms, IEEE Trans Geosci Remote Sens 42 (2004) 1377–1386.